Title

Analysis of Coastal Fog from a Ship During the C-FOG Campaign

Journal

Boundary-Layer Meteorology, 181(2-3)

ISSN

0006-8314

Authors

Wang, S
Fernando, HJS
Dorman, C
et al.

Publication Date

2021-12-01

DOI

10.1007/s10546-021-00667-5

Peer reviewed

Boundary-Layer Meteorology
https://doi.org/10.1007/s10546-021-00667-5

RESEARCH ARTICLE

Analysis of Coastal Fog from a Ship During the C-FOG Campaign

S. Wang[1] · H. J. S. Fernando[1,2] · C. Dorman[6,7] · E. Creegan[3] · R. Krishnamurthy[1,4] · C. Wainwright[1] · S. Wagh[1] · R. Yamaguchi[5]

Received: 1 July 2020 / Accepted: 31 August 2021

Abstract

This work presents ship-based measurements of fog off St John's, Newfoundland, on 13 September 2018 during the Coastal Fog field campaign. The measurements included cloud-particle spectra, cloud-base height and aerosol backscatter, radiation, turbulence, visibility, and sea-surface temperature. Radiosonde soundings were made at intervals of less than 2 h. Fog occurred in two episodes during the passage of an eastward-moving synoptic low-pressure system. The boundary-layer structure during the first fog episode consisted of three layers, separated by two saturated temperature inversions, and capped by a subsidence inversion. The lowest layer was fog, and the upper layers were cloud. The second fog episode consisted of one well-mixed fog layer capped by a subsidence inversion. Low wind speeds and stable stratification maintained low surface-layer turbulence during fog. Droplet size distributions had typical bimodal distributions. The visibility correlated with the droplet number concentration and liquid water content. The air temperature was higher than the sea-surface temperature for the first 30 min of the first fog episode but was lower than the sea for the remainder of all fog. The sensible heat flux was upward, from sea to air, for the first 62% of the first fog episode and then reversed to downward, from air to sea, for the remainder of the first fog episode and the second fog episode. The counter-gradient heat fluxes observed (i.e., opposite to what is expected from the instantaneous air–sea temperature difference) appear to be related to turbulence, entrainment, and stratification in the fog layer that overwhelmed the influence of the air–sea temperature difference. While the synoptic-scale dynamics preconditioned the area for fog formation, the final step of fog appearance in this case was nuanced by stratification–turbulence interactions, local advective processes, and microphysical environment.

Keywords Coastal fog · Microphysics · Stratification · Synoptic effects · Turbulence

✉ S. Wang
swang18@nd.edu

Extended author information available on the last page of the article

Published online: 11 October 2021

1 Introduction

The term (liquid) fog refers to a condition where near-surface visibility drops below 1 km due to suspended small water droplets that scatter light (AMS 2012a, b, c, d). A historic account of marine-fog research is given in Lewis et al. (2003), starting from the early ship-based observations of Taylor (1917), which took place near the area of the study described in this paper. There is continued scientific interest in fog because the difficulty of accurately forecasting its location and onset time, and its duration affects applications such as transportation hazards, ecology, and defence (Fernando et al. 2020). In a ship-observation-based climatological study of worldwide marine-fog occurrence, Dorman et al. (2017) found that the greatest fog occurrence is in the Northern Hemisphere in the north-western oceans, including the Grand Banks, which was examined mostly in a synoptic-scale perspective by Isaac et al. (2020), and is examined at a local scale as part of the Coastal Fog (C-FOG) field campaign (Fernando et al. 2020 for the C-FOG overview and Gultepe et al. 2021 for a review on microphysics during C-FOG).

Many types of fog have been identified based on formation mechanisms, location, dynamics, and timing (Gultepe et al. 2007, 2016). Based on the formation mechanism, major fog types are radiative fog (caused by nocturnal cooling of the surface, occurring mainly over land), advection fog (caused by modification of air masses moving over water bodies), and mixing fog (caused by turbulent mixing of nearly saturated warm and colder air masses to produce supersaturation over water or land) (Taylor 1917). These may be subdivided into a marine fog, defined as fog over the open ocean (open-ocean fog), over marginal and shallow seas (sea fog) or in the coastal zone where air over a land mass and ocean interacts (coastal fog) (reviewed in Koračin et al. 2014). Further, marine fog may be subdivided into a cold-sea fog when the sea surface is colder than the air or a warm-sea fog when the sea surface is warmer (Kim and Yum 2010).

The study of marine fog is challenging due to the extreme range of scales and number of processes involved (Koračin et al. 2014; Gultepe et al. 2017). Contributors from the atmospheric realm include: (1) synoptic (large-scale) weather systems; (2) mesoscale fronts, advection, convection, convergence, subsidence, cloud-fog nexus; (3) microscale aspects such as instabilities and turbulence, fluxes of latent and sensible heat, momentum, water vapour and aerosols, and longwave and shortwave radiation; and (4) microphysical and thermodynamic processes involving hygroscopic aerosols and water droplets. Background stratification also plays a crucial role by affecting turbulence (Heo and Ha 2010). On the ocean side, the upper ocean has the most impact, and sea-surface temperature (SST), upper mixed-layer turbulence, temperature/salinity distribution, marine aerosols, and mesoscale coastal circulation all can be important.

warm-sea fog observations date back to Petterssen (1938), followed by copious literature on Californian coastal fog observations (reviewed in Koračin et al. 2014). Instability in the surface layer due to a superadiabatic temperature gradient may produce convective turbulence, causing the mixing of saturated warm surface air with near-saturated colder air aloft to produce 'mixing fog' that evolves under convective forcing and cloud-top cooling (Kim and Yum 2017). A comparative study of warm versus cold-sea fog along the south China coast concluded that, contrary to earlier findings, the top of warm sea fog may extend above the inversion base (Huang et al. 2015). Coupled modelling by Kim et al. (2020) showed that not only air–sea coupling but also external factors such as advection may determine warm-sea fog formation.

The aim of this study is to shed light on the formation, maturation, and dissipation of fog during a warm-sea fog coastal event observed from a research vessel (R/V *Hugh R. Sharp*) off St John's, Newfoundland, on 13 September 2018 during the C-FOG campaign. Section 2 outlines the campaign and data collection. A synoptic overview of conditions during the observational period is given in Sect. 3, followed by in situ, profiling, radiation, microphysical, and microscale observations in Sect. 4, and a discussion of results and conclusions in Sects. 5 and 6, respectively.

2 Measurements, Settings, and Analysis

We focus on measurements made by the R/V *Hugh R. Sharp* while off the coast of St. John's, Newfoundland (Fig. 1) between 1700 UTC 12 September 2018 and 0700 UTC 13 September 2018. This period is defined as the first ship intensive operational period (SIOP 1; Fernando et al. 2020) and is referred to as the event period here. The ship left St. John's Port on 1200 UTC 12 September, following the track in Fig. 1. Along the way the ship encountered fog and adjusted the course to optimize the sampling of the fog that covered an area about 80 km in the south–north direction and 20 km in the west–east direction.

Instruments used on the ship are shown in Fig. 2 and are listed with accuracy and sampling rates in Table 1. The bow mast had temperature (T_{air}) and relative humidity (RH)

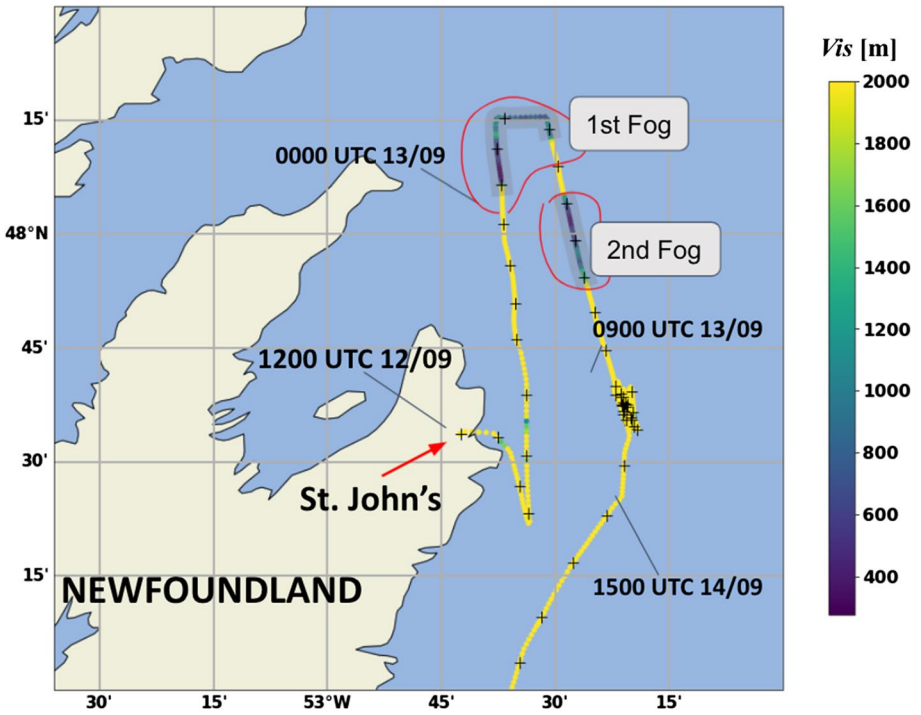

Fig. 1 Coloured dotted line indicates the visibility (m) clipped at 2000 m along the ship track for the present analysis from 1200 UTC 12 September to 0000 UTC 15 September 2018, with + marking the ship location at the start of each hour

Fig. 2 Instrument positions on-board the R/V *Hugh R. Sharp* and pictures of key instruments taken during the campaign relevant to the present study. Adapted from Fernando et al. (2020)

probes (HMP155, Vaisala, Helsinki, Finland) at 7 m, 9 m, and 12.5 m above sea level (a.s.l.), a broad band net radiometer (K&Z CNR4, Kipp & Zonen, Delft, Netherlands) at 11.5 m a.s.l. for upward and downward longwave and shortwave radiation, and a three-dimensional sonic anemometer (CSI IRGASON, Campbell Scientific, Logan, Utah, USA) at 12.5 a.s.l. for turbulence and fluxes. On top of the pilot house at about 9.1 m a.s.l. was a visibility and present weather detector (PWD 22, Vaisala, Helsinki, Finland), and a fog monitor (FM-120, Droplet Measurement Technologies, Longmont, Colorado, USA) that measures fog droplet spectra and reports calculated fog droplet statistics. A ceilometer (CL31, Vaisala, Helsinki, Finland) was between the pilot house and exhaust stack on the deck at 4.5 m a.s.l. A GPS-based radiosonde system (RS41-SGP, Vaisala, Helsinki, Finland; MW41, Vaisala, Helsinki, Finland) made profiles of the atmosphere as the sonde ascended and descended. Ten up-and-down profiles were made from 1721 UTC 12 September to 1130 UTC 13 September. The bulk SST was measured at 1–3 cm depth with a SST sensor (sea snake) consisting of a chain of floating thermistors (YSI 46040, YSI, Yellow Springs, Ohio) and held about 2 m away from the side of the ship by a boom near the pilot house. All motions of the ship, including pitch, roll, yaw, and horizontal movement, were measured by an inertial navigation system (VN100, VectorNav, Dallas, Texas; Trimble BX982 Dual-GNSS receiver, Trimble, Sunnyvale, California) and used for motion correction.

Turbulence variables were derived using a Reynolds-averaging method as well as a spectral and wavelet transform analysis (Tennekes and Lumley 1972; Farge 1992; Torrence and Compo 1998; Cuxart et al. 2002; Terradellas et al. 2005; Aubinet et al. 2012).

Table 1 Instruments on R/V *Hugh R. Sharp*

Instrument, system and platform	Measured and retrieved parameters	Related information
Bow mast: three levels of HMP155 T/RH probes (7, 9, and 12.5 m); CSI IRGASON at 12.5 m from the mean sea level; K&Z CNR4 net radiometer at 11.5 m from the mean sea level; VectorNav VN100 IMU and Trimble BX982 Dual-GNSS receiver for motion correction	Three components of velocity (u_x, u_y, u_z), temperature (T_{air}), relative humidity (RH), CO2 and H2O fluxes, radiation (including downwelling and upwelling longwave and shortwave radiative fluxes)	CSI IRGASON 1 mm s^{-1} (for u_x, u_y), 0.5 mm s^{-1} (for u_z), 0.025 °C (for sonic temperature), 0.6° (for wind direction); HMP155 ± 1.8% (RH), ± 0.25 °C (T_{air}) (Acy), 1 Hz Dar; CNR4 ± 10 W m^{-2} or 1% (Acy), ± 1 W m^{-2} (relative Acy), 6 s, 1-min averages (Dar)
Vaisala CL31 ceilometer	Cloud/fog base height and aerosol backscattering, three-cloud layers	0–7.5 km (Ran), 5 m (Res), 3 s (Dar)
PWD22 visibility sensor[a]	Visibility (Vis) and precipitation	± 10% (Acy), 10 m–10 km (Ran)
Fog monitor FM120, cloud-particle spectrometer[a]	Fog droplet spectra is used for droplet number concentration (N_d), mean volume diameter (*MVD*) effective diameter (D_{eff}), liquid water content (*LWC*), and visibility (Vis)	Droplet size: 2–50 μm (Ran)
Vaisala RS41-SGP radiosonde launches and DigiCORA Sounding System MW41	Meteorological profiles of pressure (*P*), air temperature (T_{air}), relative humidity (RH), wind speed (*S*), and wind direction (*WDir*)	hPa (*P*), 0.5 °C (T_{air}), 5.0% (RH), 0.15 m s^{-1} (*S*), 2° (*WDir*) (Acy); 0.1 hPa, 0.1 °C, 5.0%, 0.1 m s^{-1}, 0.1° (Res); 3–1080 hPa (*P*), − 90 ± 60 °C (T_{air}), 0–100% (RH), 0–160 m s^{-1} (*S*), 0–360° (*WDir*) (Ran)
Sea snake system	SST (bulk) at 1–3-cm depth via a chain of floating thermistors	0.1 °C (Acy)

Acy, accuracy; Dar, data rate; Ran, range; Res, resolution

[a]Instrument located at the bridge (≈ 9.7 m above the mean sea level)

These include (a) turbulence kinetic energy (TKE, e) and the dissipation rate of TKE (ε) (using TKE spectra); (b) sensible heat flux (SHF); and (c) latent heat flux (LHF) (both using eddy-covariance method).

The three-hourly North American Regional Reanalysis (NARR) with a 32-km grid-point separation (https://psl.noaa.gov/cgi-bin/data/narr/plothour.pl, Mesinger et al. 2006) was used to explore the synoptic setting. The data are from the Research Data Archive at National Center for Atmospheric Research (NCAR) (National Centers for Environmental Prediction, National Weather Service, NOAA, U.S. Department of Commerce 2005).

Additional details about the ship and the C-FOG campaign are presented in Fernando et al. (2020).

3 Synoptic Overview

Fog occurred at the ship during 0000–0315 UTC and 0450–0650 UTC on 13 September 2018 when it was north to north-north-east of St John's, Newfoundland (Fig. 1). This section presents the synoptic setting for these events.

An eastward-moving synoptic scale cyclonic system forced the fog occurrence and the conditions around it. This sequence is well represented by the NARR sea-level pressure (SLP) analyses. At 1800 UTC 12 September the low centre was over the south Newfoundland coast (Fig. 3a). On the south-eastern–eastern side of the low, the isobars were closest together and the 10-m winds were the strongest and from the south. On the west side of the low centre, the winds were weakest and from the north. This structure about the low remained the same throughout this event. The low continued eastward, crossing the eastern Newfoundland coast around 0000 UTC 13 September and turned south-east. At 0300 UTC 13 September, the low centre was at its lowest pressure, east of the coast, south of the ship while at the ship the 10-m winds had switched to the north-east (Fig. 3b). At this time, the first fog event was ending and the second started 2 h later. The low continued to the south-east so that by 1200 UTC 13 September, the low had drawn farther away from Newfoundland and the central pressure had increased.

The moisture in the boundary layer, a crucial aspect for fog, is represented by the NARR 2-m RH sensor. Throughout this event, the RH maximum area extended roughly north to south across the low centre, moved with the low, and the highest values occurred over the ocean. At 1800 UTC 12 September the highest relative humidity extended from the southern Newfoundland coast toward the south (Fig. 3d). At 0300 UTC 13 September, the relative humidity greater than 95% is a complex pattern that included the eastern Newfoundland coast and waters (Fig. 3e). The maximum value of RH, which was greater than 98%, included portions over water around eastern Newfoundland and especially around the southern Avalon Peninsula, while the value of RH over land was lower. At this time, the ship was on the edge of this RH maximum and was near the end of the first fog event. By 1200 UTC 13 September, the RH maximum had drawn eastward from Newfoundland and separated into a northern portion and a smaller, weaker southern portion in the low centre (Fig. 3f). At this time, the humidity had fallen below 95% over the eastern Newfoundland waters and the ship.

The atmosphere capping the surface layer is represented by the 700-hPa geopotential height (near 3 km elevation) and wind speeds. The closed structure of SLP transformed to an open wave at 700 hPa. At 1800 UTC 12 September, a north–south trough axis was across the Newfoundland coast and the SLP low centre (Fig. 3g). The trough crossed the

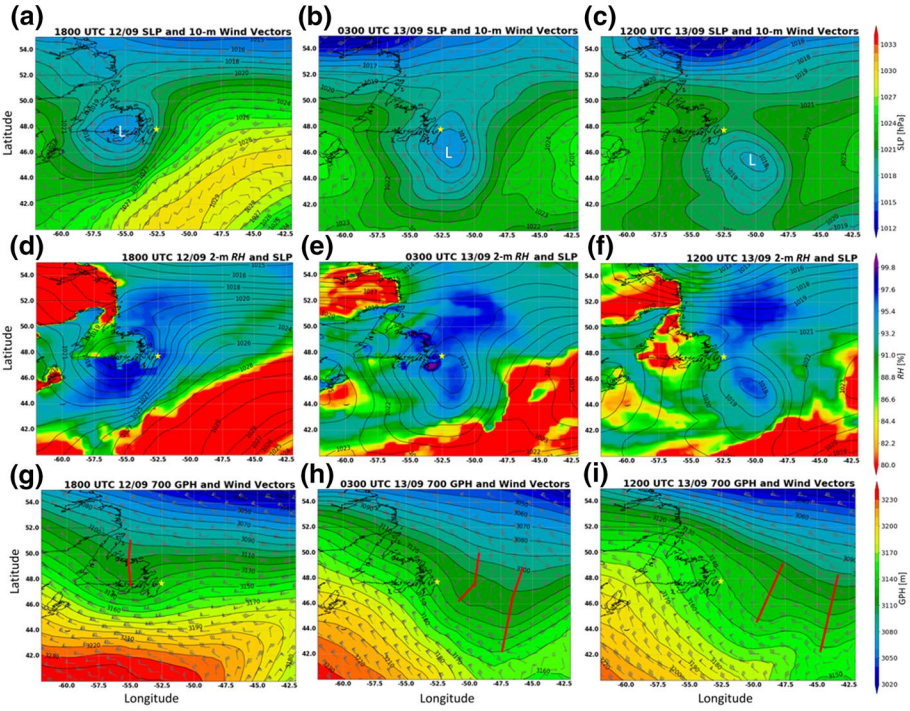

Fig. 3 North American Regional Reanalysis (NARR) SLP with 1 hPa isobar spacing (shaded colour), 10-m wind vectors and L the low centre (**a**), 2-m RH (shaded colour) and SLP (**b**), and 700-hPa geopotential height (GPH, shaded colour) and wind vectors (**c**), for 18 UTC 12 September, 0000 UTC 13 September and 12 UTC 13 September. Star marks the ship location, and the red lines mark the troughs in 700-hPa geopotential height

coast with the low and broadened into two axes: the western axis was over the eastern side of the deepened low at 0300 UTC 13 September (Fig. 3h) and the second axis was farther to the south-east and separated from the first axis by a weak anticyclonic ridge. By 1200 UTC 13 September, the broad trough with its two axes had moved farther to the south-east (Fig. 3i). At the same time, an anticyclonic ridge had moved over the west coast of Newfoundland, increasing subsidence over the broader area and the ship. Before the trough axis passed, the 700 hPa winds over the ship were from the west. After passage, they were from north–north-west ((Figs. 4, 5).

Geostationary Operational Environmental Satellite (GOES) East satellite infrared images showed that a band of higher clouds was over the east side of the SLP low. At 1745 UTC 12 September, a cloud band extended from the north-east, then along the east side of the surface low, over the ship, and then to the south-west (Fig. 4a). This band shifted eastward, so that by 0245 UTC 13 September the band was well east of Newfoundland (Fig. 4b). However, over the eastern coast of Newfoundland and the ship is a faint dark area supporting a low cloud overcast, which radiates on the edge of the infrared band. This low cloud overcast (i.e., imminent fog) over the ship and on the western side of the infrared band is confirmed by the ship's soundings and ceilometer data (see Sects. 4.2 and 4.3), the surface observations at St John's airport, as well as the visual images before dark (not

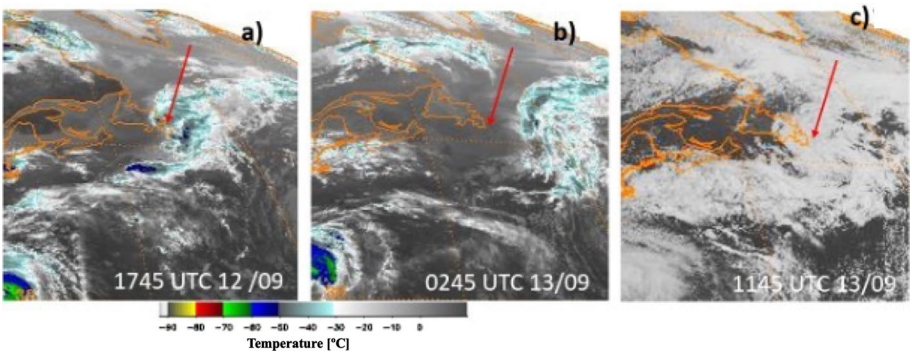

Fig. 4 Geostationary operational environmental satellite (GOES) east infrared images for 1745 UTC 12 September (**a**), and 0245 UTC 13 September (**b**), and visual image for 1145 UTC 13 September. The temperature colour bar is for infrared cloud top temperatures, and the arrow points to ship location which was entering fog during **b**

shown) and after sunrise (Fig. 4c, 1145 UTC 13 September). Thus, during the ship fog events, there was a low stratus overcast with air clear above.

Back trajectories are now presented, as they reveal important details about the air parcel history (Table 2) computed from the Hybrid Single-Particle Lagrangian Integrated Trajectory (HYSPLIT) model (Draxler and Hess 1997). The horizontal advection relative to the SST was significant. To the south of the ship, SST isotherms were oriented along the 280°–100° direction. Neutral surface advection was assumed to be oriented within + or − 20° of this SST isotherm alignment. Warm air advection (warmer air over colder water) would have been from 120° to 260°. All 24-h back trajectories for air close to the sea surface (10 m and 100 m) were from 165° to 186° (Table 2) which was well in the central portion of the warm advection sector. However, in the last 3 h of all back trajectories ending after 0000 UTC 13 September and below 600 m came from the south, passed the ship and reversed direction so as to arrive at the ship from the north.

The last 6 h of the back trajectories were examined for changes in elevation (Table 2). During the first fog event, the air parcels at and above 100 m in the fog layer increased in elevation as expected in a cyclonic system. However, the 100-m parcels in the second (shallower) fog event did not significantly change elevation. Subsidence during the last 6 h of the back trajectories occurred first at 3000 m at 0000 UTC and lower elevations later so that subsidence extended down to 400 m at 0600 UTC 13 September.

4 Ship Observations

4.1 Surface Observations

One-minute averages of the ship's surface meteorological observations from 1500 UTC 12 September to 1000 UTC 13 September are presented to illuminate the conditions for the fog event (Fig. 5). Based on the visibility (Vis) being less than 1000 m, the first fog episode lasted from 0000 to 0315 UTC 13 September, with two short periods of visibility less than 1000 m. The second fog episode was from 0450 to 0650 UTC 13 September with one short visibility decrease to less than 1 km. The lowest value of *Vis* during the first episode was

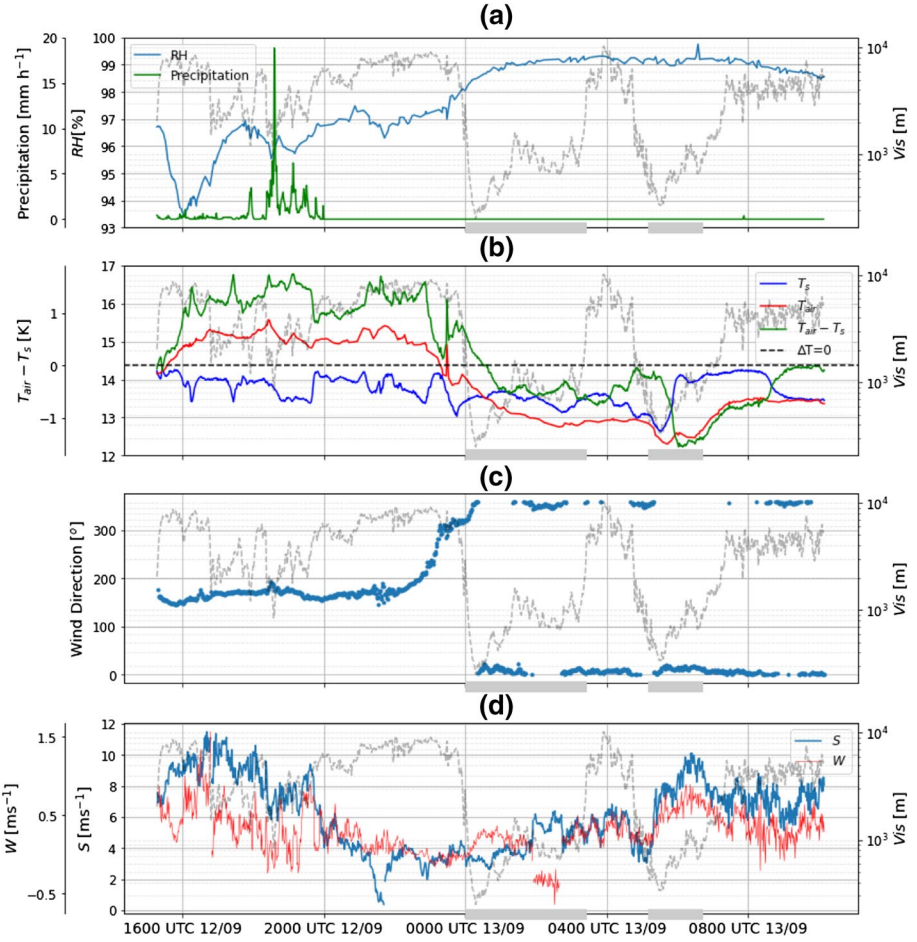

Fig. 5 Overview of selected measured variables during the event period. Grey (shaded) dashed line in all plots is visibility in metres. Variables are presented as 1-min average unless stated otherwise. **a** Relative humidity (RH), precipitation in mm h^{-1}. **b** Air temperature (T_{air}) and SST (T_s) from the Sea Snake, **c** wind direction, **d** wind speed (S), and the vertical velocity component (W)

≈300 m at 0020 UTC and during the second episode it was ≈330 m at 0530 UTC. However, between the two fog episodes the visibility increased to 10,000 m.

Moisture is an important factor in fog development. The value of RH was 97% at the start of the first fog event, and it increased to near 99% and remained so for several hours, including during non-fog conditions. Precipitation, often associated with fog (Gultepe and Milbrandt 2010), did not occur with fog nor within 3 h of it.

Near-surface temperatures are critical to fog, but especially for stability. Air temperature was measured by the 12.5-m bow mast probe (T_{air}), the SST was measured by the Sea Snake, and their difference ($\Delta T = T_{air} - T_s$), was computed (Fig. 5b). Before the fog, $T_{air} \approx 1$ °C greater than the value of SST as the surface air was from the south. The value of T_{air} decreased starting around 2300 UTC 12 September and continued falling until after 0100 UTC 13 September as the wind direction shifted to more northerly. At the same time, the SST remained relatively constant. The effect was that ΔT was positive for the first

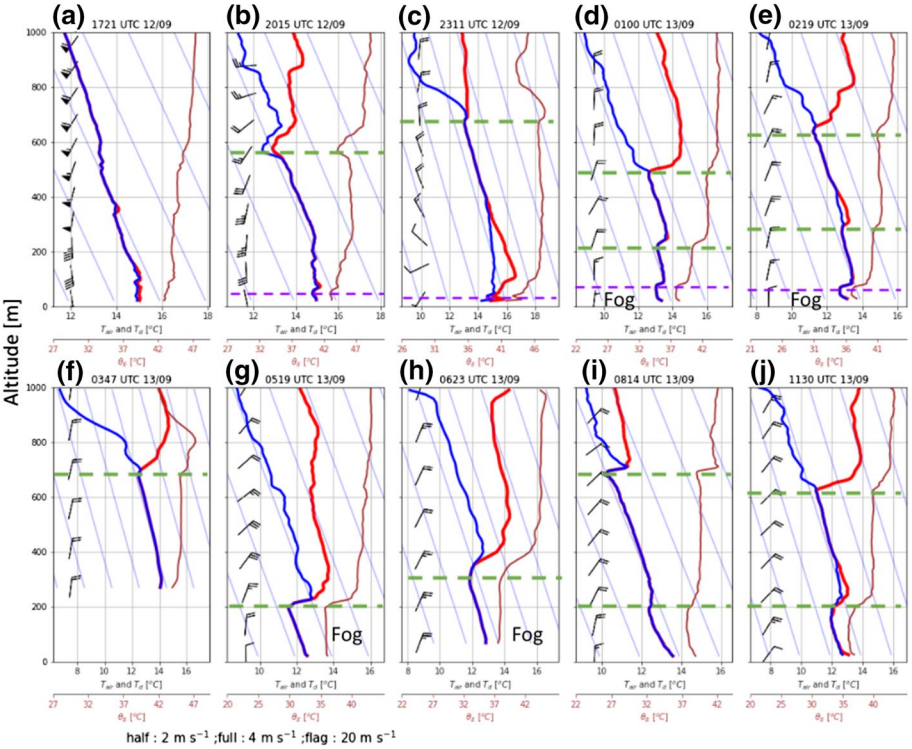

Fig. 6 Ship radiosonde soundings for air temperature (red), dew point (blue), and equivalent potential temperature (brown). Wind barbs also shown: half barb is 2 m s^{-1}, full barb is 4 m s^{-1}, and flag is 20 m s^{-1}. Horizontal dashed green line indicates a saturated, air temperature inversion base height. Horizontal dashed purple line marks the base height of the near-surface saturated inversion. Faint blue lines in the background are moist adiabatic lapse rates

30 min of the first fog event, changed sign, and remained negative for the remainder of the fog events. There was a sharp increase in the SST halfway through the second fog event, causing a sharp decrease in the temperature difference ΔT. Thus, the difference ΔT was unstable for the second half of the first fog event and all of the second fog event.

Winds were southerly at the beginning of the time series but switched to northerly with initialization of the first fog event as the low crossed the coast and remained so during the fog events. The wind speed decreased to a minimum before the first event and remained low until the start of the second fog event when it increased. These low speeds were in the north-west portion of the low and the increase was associated with the low moving farther to the south-west. The vertical velocity component followed a pattern similar to that of the wind speed.

4.2 Radiosonde Profiles

Radiosondes launched from the ship provide detailed profiles that show the evolution of the lower atmospheric structure and fog layer (Fig. 6). To increase the number of vertical profiles, some of the helium-filled balloons were not fully sealed intentionally so that each launch produced two profiles approximately 1 h apart: the balloon ascended while leaking

Table 2 Results from the HYSPLIT 24-h back trajectories from the ship at different heights listed in the top row

Time Day	10 m		100 m		400 m		600 m		1000 m		3000 m	
	(°)	(km)	(°)	(km)	(°)	(km)	(°)	(km)	(°)	(km)	(°)	(km)
1800 UTC 12	183	500	178	540	175	660	180	730	190	840	193	910
2100 UTC 12	177	525	177	575	190	600	180	700	182	750	205	830
0000 UTC 13	175	610	178	680	185	720	185	730	190	750	240	950
0100 UTC 13	176	625	180	660	185	665	190	700	193	720	280	900
0200 UTC 13	176	600	178	660	183	670	186	700	190	800	295	1000
0300 UTC 13	178	590	180	595	190	600	190	710	195	830	320	1000
0400 UTC 13	182	580	186	600	190	630	190	730	192	820	320	1010
0500 UTC 13	178	550	183	620	190	670	195	720	200	810	316	1050
0600 UTC 13	178	550	183	598	188	690	183	750	190	800	315	1100
0900 UTC 13	165	450	168	570	180	570	193	700	197	750	320	1050
1200 UTC 13	167	480	170	550	188	600	190	680	205	650	310	970

For each trajectory, a compass direction is posted relative to north in a clockwise sense and the distance to the end of the 24-h backtrack. Enclosed in the green border are elevations within a fog or cloud layer during the first fog episode (the larger) and a fog layer in the second fog episode (the smaller). Colours signify vertical change over the last 6 h of the backtrack. Light blue is up < 250 m, blue is up 250–500 m, dark blue is up > 1000 m, yellow is no significant change, and pink is down < 225 m, orange is down 225–550 m, and red is down > 550 m

out helium, and after rising to a height covering a good part of the boundary layer, the balloon descended. Owing to horizontal drift, the ascending and descending tracks in these cases are significantly different. The radiosonde profiles of both ascending and ascending/descending modes are shown in Fig. 6, and those taken during the descending phase are at 0347 and 0623 UTC 13 September. Profiles with at least 70% data availability were selected for this presentation, resulting in a total of 10 profiles of air temperature (T_{air}) and dew point (T_d) with horizontal wind profiles shown as wind barbs.

The air temperature, dew point, and wind speed are shown with elevation in each frame of Fig. 6. Moist adiabatic lapse rates are in the background for comparison as most of the sounding profile lapse rates are close to this. Also shown is the equivalent potential temperature (θ_e), which is the temperature reached if all of the water vapour of a parcel were condensed, releasing its latent heat and the parcel brought adiabatically to 1000 hPa. When θ_e is constant with elevation, or the air temperature of a saturated parcel follows the moist adiabatic lapse rate, the air parcel is neutrally stable and can move vertically without the loss or gain of energy, which is so for major portions of the soundings shown.

The soundings are complex with θ_e neutral or near-neutral layers interspersed with θ_e inversions (Fig. 6, Table 3). After 1721 UTC 13 September, a saturated or near-saturated surface layer below 1 km elevation is capped by an air temperature and θ_e inversion with a dry layer (Fig. 6b–j). There is yet another such inversion and dry layer around 3 km for each sounding, which is not shown as it is not directly related to the surface-layer structures.

Late on 12 September (Fig. 6b, c) there was a deep saturated or mostly saturated cloud layer around 600 m deep and a shallow surface-layer inversion. Initially, surface winds were from the south, as were the back trajectories (Table 2), which was warm-air advection over colder water but without fog at the ship.

The winds shifted before 0000 UTC from south to west to north (Fig. 5c) and initiated the first fog event, which had two θ_e neutral layers (Fig. 6d, e). These layers were separated by a saturated inversion and the top layer had a subsidence inversion cap. A third saturated

Table 3 Equivalent potential temperature (θ_e) inversions based on radiosonde profiles in Fig. 6

Fig. 6	Time Date	Latitude	Longitude	Base height [m]	Top height [m]	$\Delta\theta_e$ [K]	N [s^{-1}]	Ri_b
b)	2015 UTC 12/09	47.77	-52.59	41	69	1.40	0.039	0.57
				560	656	4.30	0.037	1.40
c)	2311 UTC 12/09	48.02	-52.61	34	138	4.30	0.036	6.70
				660	692	1.20	0.034	1.51
d) Fog	0100 UTC 13/09	48.17	-52.63	67	88	1.70	0.050	0.81
				218	246	1.90	0.046	2.63
				464	566	1.85	0.024	1.16
e) Fog	0219 UTC 13/09	48.25	-52.59	60	77	2.26	0.065	4.20
				256	299	1.27	0.030	4.32
				632	678	1.83	0.035	5.17
f)	0347 UTC 13/09	47.51	-52.00	No data below 300 m				
				672	798	2.29	0.024	122.09
g) Fog	0519 UTC 13/09	48.07	-52.48	187	226	4.5	0.060	3.24
h) Fog	0623 UTC 13/09	47.58	-52.17	282	405	5.05	0.036	117.13
i)	0814 UTC 13/09	47.83	-52.41	180	250	1.40	0.025	1.50
				679	701	3.10	0.066	19.34
j)	1130 UTC 13/09	47.59	-52.34	129	226	4.10	0.037	4.08
				611	701	3.00	0.032	18.5

Character in the left column is the panel label. Red denotes a fog sounding, yellow is saturated surface wind layer inversion, orange is saturated inversion between fog layers, and white is an inversion capping a surface-layer complex

layer was a shallow surface fog layer capped by a saturated inversion. This shallow surface layer had an irregular profile indicating a state of transition as the surface-layer back-trajectory originated from the south, passed the ship to the west, turned clockwise, and arrived at the ship from the north. By the time of this sounding, the falling air temperature was close to the SST. On 0219 UTC 13 September (Fig. 6e), the fog event continued with the

two neutral layers, but thicknesses increased while sandwiched by three inversions. At this time, the surface air temperature was lower than the SST.

The structure of the second fog event soundings (Fig. 6g, h) was substantially different from the first, and consisted of a single neutral, saturated fog layer, 200–300 m deep, capped by an inversion. This was a mixed layer caused by wind shear and convection as the sea surface was warmer than the air (Fig. 5b). The second sounding during this fog episode (Fig. 6h) was similar to the first, except that the surface mixed layer was deeper and the winds stronger.

The sounding structure was different after the second fog event (Fig. 6i). The saturated surface layer lifted to be a stratus layer capped and footed by saturated inversions and the wind from the north-east. Below was a fog-free, saturated surface layer that was unstable in the lower half as the surface winds were from the north and the SST was higher than the air temperature. The next sounding (Fig. 6j) was similar. Although saturated, the bottom layer was devoid of fog, possibly due to higher wind speeds and greater turbulence (Sect. 4.6).

The change of base-to-top thickness of the capping (θ_e) inversion layer for the second fog episode was more than twice that of the first (Table 3). The Brunt–Väisälä frequency (N) and the bulk Richardson number (Ri_b) were calculated in bulk values and presented for comparison, which differ significantly, and are defined as

$$N = \left(\frac{g}{\theta_e} \frac{\Delta\theta_e}{\Delta z} \right)^{\frac{1}{2}},$$

and

$$Ri_b = \frac{\left(\frac{g}{\theta_e} \right) \Delta\theta_e \Delta z}{(\Delta U)^2 + (\Delta V)^2},$$

respectively, where g is the acceleration due to gravity, θ_e is the ambient equivalent potential temperature, $\Delta\theta_e$ is the equivalent potential temperature difference across inversion, Δz is the thickness of inversion, ΔU and ΔV are the eastward and northward vertical velocity differences over Δz. The large values of the bulk Richardson numbers in soundings (Fig. 6f, h) were due to variations in the bulk velocity shear across the inversion.

4.3 Ceilometer Observations

The ceilometer aboard the ship recorded the backscatter profiles of the range-corrected signal, from which the height of cloud bases, inversion bases and atmospheric properties over time could be determined (Kotthaus et al. 2016). Figure 7a shows the ceilometer profile for 1200 UTC 12 September to 1000 UTC 13 September covering the event period. The great range of return from the surface to 2000 m over the period 1900–2000 UTC 12 September marks the passage of the eastern side of the low and elevated mixing by near-surface shear (Fig. 5d). The base of the two fog events (horizontal white bars) elicited maximum backscatter near the surface (0000–0315 UTC, 0450–0650 UTC 13 September).

The initialization of the first fog event was a complex, multilevel event and thus its visualization is expanded for better viewing and plotted with the Vis time series to identify the relationship to this variable (Fig. 7b). An elevated stratus cloud base appeared at 600 m at 2250 UTC 12 September. The height of this layer had wavelike oscillations (possibly interfacial waves) at the inversion (Fig. 6c, d) and the base descended to

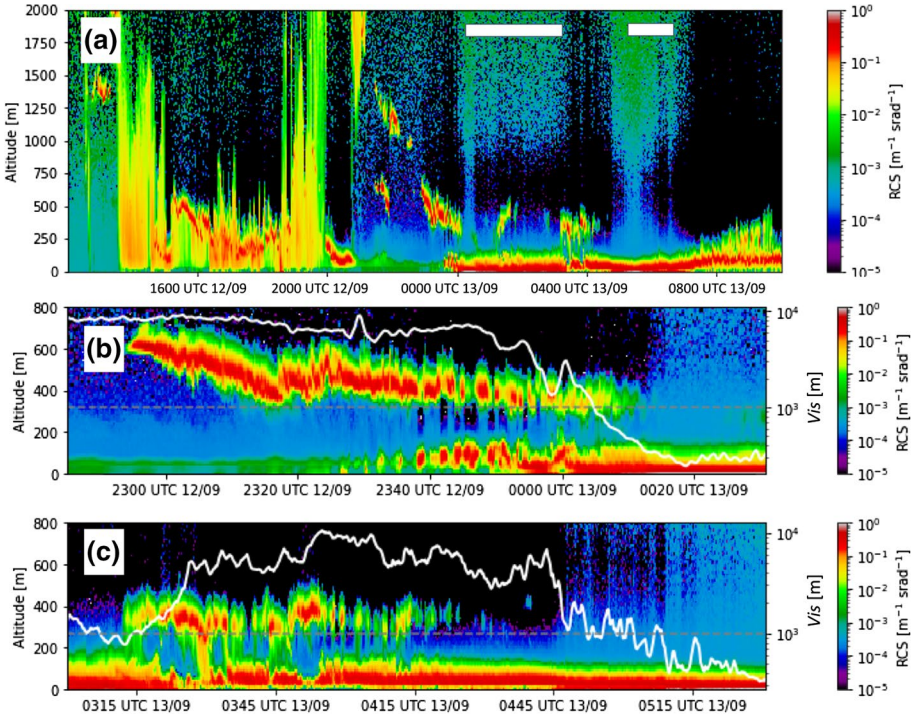

Fig. 7 **a** Ceilometer backscatter profile of reported range-corrected signal (RCS). Horizontal white bars mark the two fog occurrence events. Red colours indicate the highest backscatter indicating a cloud base. **b**. Ceilometer backscatter profile of RCS and Vis around the start of first fog event. Red colours indicate the highest backscatter, indicating a lower and an upper cloud base. **c** Ceilometer backscatter profile of RCS and Vis during the break between the two fog events. Red colours indicate the highest backscatter, indicating a lower and an upper cloud base

300 m. The backscattering strength of this faded after about 0000 UTC 13 September due to the formation of an overcast surface layer and then fog that blocked the signal to the upper layer. A separate surface layer began forming around 2330 UTC in patches that joined together to form a fog layer with Vis < 1000 m around 0000 UTC 13 September. The patchiness suggests that this layer was formed locally rather than advected as a block. It is discussed below that a third layer formed by differential advection pushed into the space between the surface layer and the lowering stratus layer and was separated from both by saturated air temperature inversions. In summary, after 0000 UTC 13 September there were three layers separated by two inversions.

A second complex, multilevel event occurred in the break between the two fog events, which is also expanded for better viewing and plotted with the Vis time series for reference (Fig. 7c). Between 0315 and 0430, the surface visibility was well above 1 km and the near-surface layer/cloud became patchy with an elevated base above 300 m (Fig. 6f; there was no data below this height). Near-surface conditions allowed the ceilometer to probe an upper cloud scattering layer that was based 200–350 m a.s.l. and exhibiting wave-like behaviour. The ceilometer signal scattered back from this cloud weakened with time and disappeared by 0430 UTC even though the surface visibility remained

high, suggesting that the layer was replaced by a subsiding dry layer supported by the 0519 UTC sounding (Fig. 6g) and the back trajectories (Table 2).

Fog returned at 0450 UTC when the near-surface cloud lowered to the sea surface and visibility decreased below 1 km. The fog layer had a capping subsidence inversion (Fig. 6g, h) and lasted until 0650 UTC when the surface scattering layer base lifted (Fig. 7a) and visibility increased above 1 km.

4.4 Broadband Radiative Flux Measurements

The net shortwave radiation (*SWNet*), net longwave radiation (*LWNet*), and total radiation (*RadNet*) was measured at 11.5 m a.s.l. on the bow mast. These are presented with visibility (*Vis*) in Fig. 8. The downward shortwave signal was modulated by the eastward moving overcast clouds late on 12 September and was zero from sunset (2149 UTC 12 September) to sunrise (0905 UTC 13 September). The *LWNet* value had a large negative maximum between 2100 and 2200 UTC 12 September when breaks in the cloud cover allowed longwave radiation to exit to space. However, from 0000 to 1200 UTC 03 September, the *LWNet* value was near zero as expected on account of the fog events or a low cloud overcast (Oliphant et al. 2021).

4.5 Microphysics

4.5.1 Brief Overview of the Key Parameters

Figure 9 provides an overview of the microphysical data from the fog monitor (Table 1). Note that the fog monitor has a droplet diameter range of 2–50 μm in diameter, and therefore the reported value of *LWC* is an integrated value for that droplet range, which excludes larger droplets.

Visibility was measured by the visibility sensor using the principle of forward scattering, and the amount of scattering is proportional to the attenuation of light due to fog droplets as a bulk measurement (Vaisala 2004). A microphysical parametrization of visibility based on the theory of extinction of visible light (Gultepe et al. 2009) is

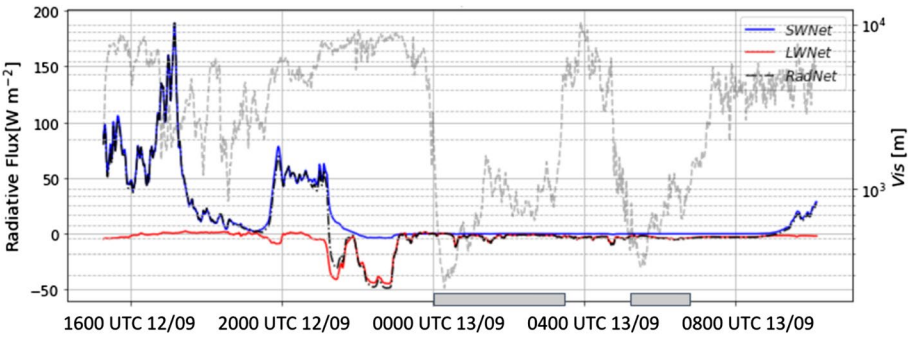

Fig. 8 Total incoming shortwave (*SWNet*), longwave (*LWNet*) radiation, and total radiation (*RadNet*)

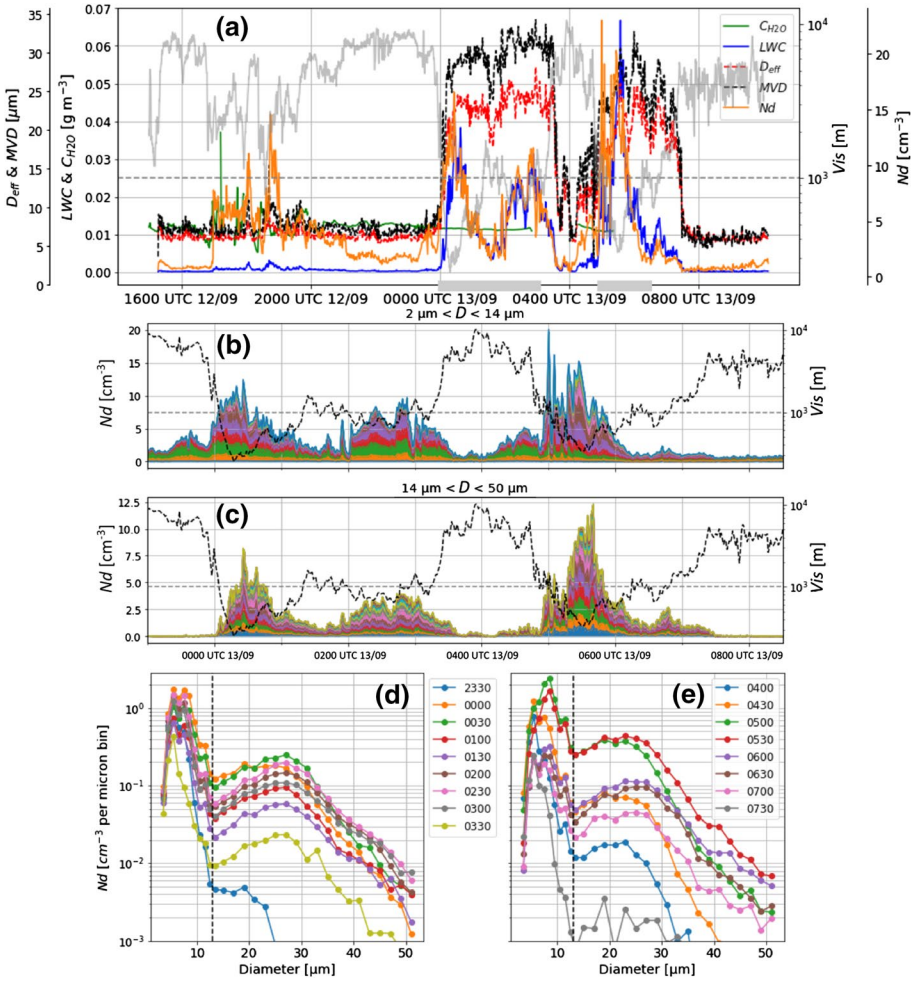

Fig. 9 **a** Liquid water content (*LWC*), vapour content (C_{H2O}), effective diameter *(ED)*, median volume diameter (*MVD*), and droplet number concentration (*Nd*) measured by the fog monitor. Right-hand side ordinate indicates the visibility level (grey solid line), and the 1-km threshold is indicated by the horizontal dashed line. **b**, **c** Number concentration for smaller (2 μm < *D* < 14 μm) and larger droplets (14 μm < *D* < 50 μm), and each micron bin labelled with a different colour. **d**, **e** Thirty-minute average of DSDs during two fog episodes, with **d** 2330 UTC 12/09 to 0330 UTC 13/09, **e** 0400 to 0730 UTC 13/09. The time period over which averaging was conducted is in the legend, and the number indicates the start of the averaging period

$$\beta_{\text{ext}} = \sum_{r1}^{r2} \pi Q_{\text{ext}}(r, \lambda) n(r) r^2 \Delta r,$$

where β_{ext} is the extinction coefficient (cm^{-1}), Q_{ext} the extinction efficiency, r the droplet radius (μm), λ the visible light wavelength (μm), $n(r)$ the particle number density (cm^{-3} μm^{-1}), and r^2 representing the surface area of the droplet.

Key variables that are measured and reported from the fog monitor are defined as below and 1-min averaged results are used in accordance with the visibility time resolution of the visibility sensor:

$$Nd = \sum_{r1}^{r2} n(r)\Delta r,$$

$$LWC = \sum_{r1}^{r2} \left(\frac{4}{3}\right)\pi\rho_{\mathrm{w}} n(r) r^3 \Delta r,$$

$$D_{\mathrm{eff}} = 2\frac{\sum_{r1}^{r2} n(r) r^3 \Delta r}{\sum_{r1}^{r2} n(r) r^2 \Delta r},$$

$$MVD = 2\left(\frac{\sum_{r1}^{r2} n(r) r^3 \Delta r}{\sum_{r1}^{r2} n(r)\Delta r}\right)^{-3} = 2\left(\frac{LWC}{\frac{4}{3}\pi\rho_{\mathrm{w}} Nd}\right)^{-3},$$

where Nd is the number concentration of droplets per unit volume (cm^{-1}), LWC the liquid water content (gm^{-3}), ρ_{w} the density of liquid water (gm^{-3}), D_{eff} the effective diameter (μm), and MVD the mean volume diameter (μm).

4.5.2 Key Observations

Figure 9a shows that during a fog period, all microphysical parameters (Nd, LWC, D_{eff}, MVD) increased significantly, with the value of Nd reaching a maximum of $\approx 15\ \mathrm{cm}^{-3}$ in the first fog episode and $25\ \mathrm{cm}^{-3}$ in the second episode, and the value of LWC reaching $0.04\ \mathrm{gm}^{-3}$ in the first and $0.07\ \mathrm{gm}^{-3}$ in the second episode. The parameters MVD and ED experienced a sharp increase from ≈7 to 30 μm (MVD) and 25 μm (D_{eff}). The increases in MVD and D_{eff} are due to the appearance of larger fog droplets, which are discussed below.

It can be observed that during the fog periods, in general, the variations of LWC and Nd are more sensitive with regard to changes in visibility compared to those of D_{eff} and MVD. However, it should also be noted that while D_{eff} (≈ 25μm) and MVD (≈ 30μm) remained relatively constant during the first fog episode, both varied more significantly during the second fog episode.

The temporal evolution of number concentration of smaller droplets ($2\ \mu\mathrm{m} < D < 14\ \mu\mathrm{m}$) and larger droplets ($14\ \mu\mathrm{m} < D < 50\ \mu\mathrm{m}$) are further explored in Fig. 9b–e, where Fig. 9b, c visualize the temporal variations with stacked number concentration values, Fig. 9d, e show the 30-min averaged droplet size distribution (DSD) for the first and second fog episodes. Bimodal DSDs were observed during the entire fog event, which was attributed to the difference between larger fog droplets and smaller fog droplets. Based on the DSD observed in Fig. 9d, e, the number concentration was divided into the smaller and the larger droplets by $D = 14\ \mu\mathrm{m}$.

Based on Fig. 9b, c, there were three periods with significant number concentration of both the smaller and the larger droplets, although the first two as a whole are considered as the first fog episode. It was previously noted that the values of MVD and ED experienced a sharp increase in fog onset and maintained a relatively steady value particularly during the

first fog episode. The reason is that in both *MVD* and *ED* formulation, the third moment of the DSD about zero (i.e. the r^3 term), equivalent to *LWC*, was more significantly attributed to the larger droplets than the smaller droplets. Therefore, as the larger droplets increased in number concentration, the parameters *ED* and *MVD* were weighted heavily towards the larger side. In addition, it can also be clearly observed that during periods of non-fog, the number concentration of larger droplets was a minimum (≈ 0 cm^{-3}) while there were still a limited number of smaller droplets. During periods of fog, there was a significant increase in the larger droplets. Hence, both the values of *MVD* and *ED* experienced a sharp increase in value at the start and end of the fog episodes.

Thirty-minute-average DSDs during the entire fog event are shown in Fig. 9d (the first fog episode) and e (the second fog episode). First, as observed in Fig. 9a–c significant increase or decrease in the number concentration of larger droplets ($D > 14$ μm) was observed as fog appeared (DSD profile 2330–0000 UTC in Fig. 9d, and 0400–0500 in Fig. 9e) and disappeared (DSD profile 0300–0330 UTC in Fig. 9d, and 0700–0730 UTC in Fig. 9e). Second, by comparing the temporal variations of the DSD profiles in Fig. 9d, e, the two fog episodes differed in both the rate of vertical translation and the statistics of the profiles. In the first fog episode (Fig. 9d), the DSD profiles are generally quite close without abrupt changes from 0000 to 0300 UTC 13 September, while significant changes were observed for the second fog episode. The more stable nature of the first fog episode was also manifested in the more stable modal diameters of the smaller (≈ 5 μm) and larger (≈ 28 μm) droplets, whereas there were observed changes in the modal diameters during the second fog episode.

It is noted that *Nd* measured during the fog events (median with 6 cm^{-3} with a maximum value 30 cm^{-3} for $LWC > 0.005$ g cm^{-3}) is low compared to previous measurements of Isaac et al. (2020) over nearby Grand Banks (median value of $Nd \approx 75$ cm^{-3}), but several differences are to be noted. First, the Isaac et al. (2020) measurements were from July to August, a period of typical cold sea fog with strong southerly winds, while ours was a warm sea fog generated by combining warmer southerly winds with cleaner, colder northerly winds within a low pressure area. Second, manufacturer-derived concentrations were used without corrections in Isaac et al. (2020), while values used in our study were corrected for wind direction and speed according to the method used by Gultepe et al. (2021). Third, it should also be noted that the fog monitor used in Isaac et al. (2020) was installed at a height of 69 m above the sea surface, which was significantly higher than the measurement heights (≈ 10 m) in this study. It should be also mentioned that the value of *Nd* from the current fog event is smaller compared to Gultepe et al. (2009, 2017).

4.5.3 Regression Analysis on Microphysical Parameters

Microphysical parameters such as *Nd*, *LWC*, and $(Nd\ LWC)^{-1}$ are known to be linearly correlated to visibility (Gultepe et al. 2009, 2017, 2021), hence a linear regression analysis is performed on the three parameters against visibility in the log space for fog periods (2330 UTC 12 September to 0800 UTC 13 September) with the results shown in Fig. 10. Regression results from (Gultepe et al. 2017) are overlaid for comparison. Note that the regression results (Table 4) reaffirm the previous results that visibility is negatively correlated with both *Nd* and *LWC*, and positively correlated to $(Nd\ LWC)^{-1}$. Particularly, *LWC* has the strongest correlation with visibility ($r = -0.85$) and *Nd* has the weakest correlation with visibility ($r = -0.61$)

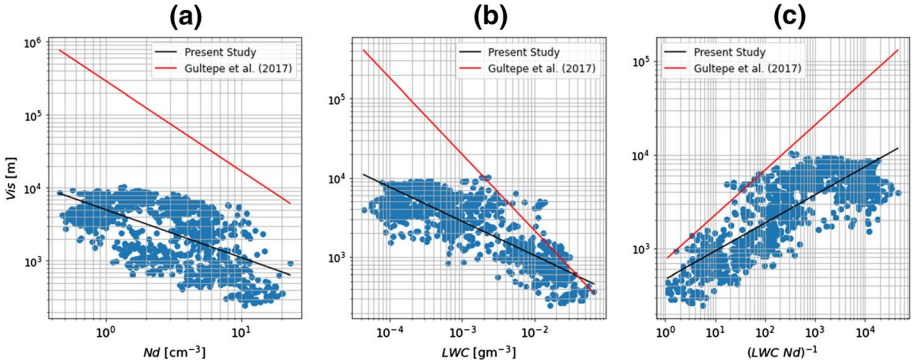

Fig. 10 Scatter plots of 1-min visibility from the visibility sensor against **a** *Nd*, **b** *LWC*, and **c** $(LWC\ Nd)^{-1}$. Black lines are the linear best-fit line (with fitting parameters in Table 4) and the red lines are previous results from Gultepe et al. (2017) for comparison

Table 4 Summary of linear regression of $y = Ax^b$ in the form of $\ln y = \ln A + b \ln x$; y is taken as visibility (m); R^2 is the coefficient of determination and *RMSE* is a measured based comparison of y in the logspace; r is the Pearson correlation coefficient

x	A	b	R^2	*RMSE*	r
Nd	5028.65	−0.66	0.37	0.57	−0.61
LWC	143.68	−0.43	0.72	0.25	−0.85
$(Nd\ LWC)^{-1}$	467.81	0.30	0.67	0.30	0.82

However, there are significant quantitative differences of the regression results in the present study and Gultepe et al. (2017). As previously noted, *Nd* observed during this fog event is significantly lower than previous results, which is also seen in Fig. 10a. In terms of *LWC*, while the two fitted lines seem to agree when fog is present ($Vis < 1$ km), they differ significantly in terms of gradients (Fig. 10b). With regard to *Nd*, the agreement is poor at all visibilities (Fig. 10a). The combined effects of the differences in *Nd* and *LWC* lead to the discrepancies observed in Fig. 10c. A more detailed investigation is required but is beyond the scope of this study.

4.6 Turbulence and Microscale Dynamics

4.6.1 Processing Techniques

Turbulence properties of wind, temperature, and moisture were measured continuously during the cruise with a three-dimensional sonic anemometer and a gas analyzer system (Table 1). The cut-off frequency for spectral analysis of turbulent fluxes were dictated by the spatial resolution (averaging length of sonic anemometer ≈0.6 m) and the Nyquist frequency (25 Hz). Two methods were employed for calculating turbulence parameters: Reynolds averaging method and wavelet transform analysis. The former is traditional, typically assumes stationarity and/or homogeneity with averaging periods selected based on the ergodicity theorem and employs Taylor's frozen turbulence hypothesis in the calculations (Tennekes and Lumley 1972; Aubinet et al. 2012).

In our case, however, the usage of Taylor's hypothesis and homogeneity could not be justified rigorously, given the significant changes of wind speed and direction sometimes observed in 1-min averages (Fig. 5c, d). Therefore, in addition, a wavelet-transform analysis was employed to examine turbulence dynamics in both space and time (Daubechies 1992; Farge 1992; Torrence and Compo 1998; Cuxart et al. 2002; Terradellas et al. 2005). The wavelet-transform coefficients were first calculated for each variable, and their conjugate products were used for the computation of coefficients corresponding to fluxes as described in Tardif and Rasmussen (2008). For wavelet transform, the TKE and fluxes were divided into three periods: below 16 s, between 16 s and 3 min, and between 3 and 10 min. The three groups were summed together within a range below 10 min (the black solid curve in Fig. 11).

For Reynolds averaging, a 15-min averaging period was used for flux calculations with data quality control conducted using conventional quality assurance and control procedures (Foken and Wichura 1996). To select an acceptable period, different averaging times (30 min, 15 min, 5 min, and 2 min) were used to compute turbulent fluxes for five variables: northward, eastward and vertical velocity components, sonic temperature, and H_2O vapor content (g m^{-3}). A threshold of 20% missing data in the time trace is set to filter out the eligible data intervals. This was necessary as there was a tendency of sonic anemometer data to drop out during thick fog. The mean values were removed from each interval with a second-order spline-fitting algorithm (Krischer et al. 2015). Abnormal peak values were removed from the detrended series with a moving window filter, which eliminates values outside 3.5 standard deviations from the mean. Variance and eddy covariances were then computed for each interval. For comparison, and considering limited data during some fog periods, 15-min and 2-min averages were computed with a 50% missing data threshold, but these data were used mainly for qualitative comparisons and the resulting data were considered as low quality.

The results from both techniques (Reynolds averaging and wavelet transform) are presented in Fig. 11. The TKE for the first fog event was very low, then increased weakly through the second fog event.

The sensible heat flux was positive or upward for 0000–0200 UTC and peaked sharply during the beginning of the first fog event. It reversed sign with a sharp downward peak and remained negative or downward for the remainder of the first fog event and all of the second fog event. The difference $T_{air} - T_s$ was positive for 0000 to 0030 UTC and negative for all fog thereafter (Fig. 5b). In contrast, the latent heat flux remained near zero for both fog events.

4.6.2 Turbulence Kinetic Energy

The TKE generally followed the trend of wind speed, which in turn translates to a steeper vertical gradient of wind speed (dS/dz) near the surface and a larger TKE production. This was evident from Fig. 11a for the pre-fog period, where TKE decayed with a reduction in wind speed starting from a secondary maximum at 2000 UTC 12 September corresponding to a wind gust (Fig. 5d). The TKE during the rain was higher but decayed thereafter. The wavelet analysis (Fig. 11a) reveals that, as expected, TKE decay was dominated by the faster decay of smaller scales (eddies), although it was unclear why the energy of larger scales did not increase during gust events. Low TKE (at around 2200 UTC 12 September) is in part due to low wind speeds from the approaching low and establishment of surface stable stratification as discussed earlier (Sect. 4.2). With the same TKE level, the visibility

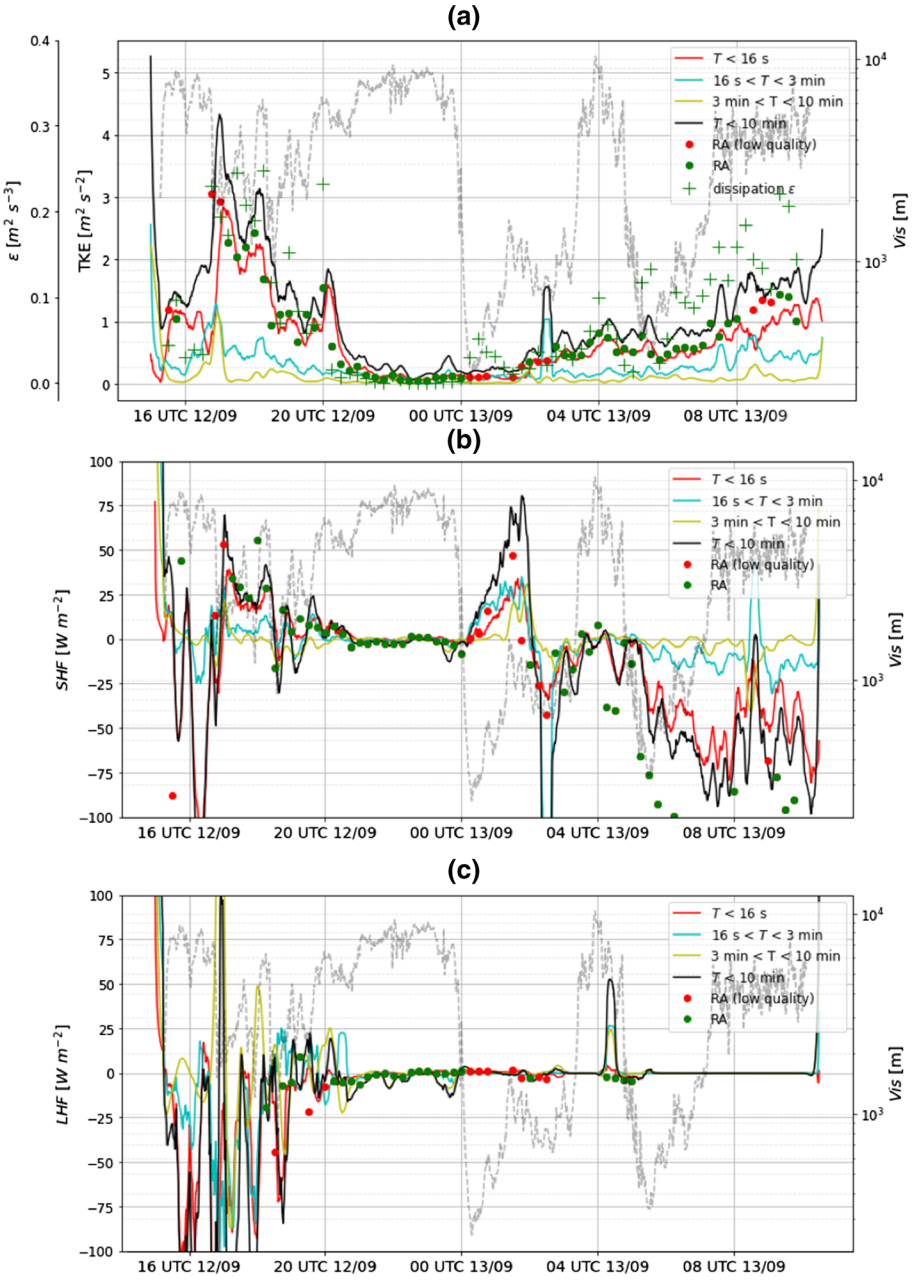

Fig. 11 Results from Reynolds averaging (RA) and wavelet transforms. **a** TKE and dissipation ϵ. **b** Sensible heat flux. **c** Latent heat flux. Visibility from the PWD-22 device is plotted as grey dashed line with the scale on the right

dropped suddenly to a minimum after midnight. Therefore, TKE or the turbulence intensity at the surface level is not a determining factor for this fog event. However, a low TKE and dissipation can be good indicators for fog when other criteria are satisfied (Gultepe et al. 2021).

The TKE during fog episodes remained small or modest (< 1 m^2 s^{-2}) with the trend of enhanced values of ε except during brief breaks. On the other hand, fog dissipation appears to be associated with an increase of TKE (0300 UTC, 0700 UTC; Figs. 6e, 11a), which is consistent with Gultepe et al. (2021). This TKE increase during the fog dissipation phase could be mainly attributed to wavelets of period < 3 min, indicating the dominant role of smaller and intermediate scale eddies of the atmospheric boundary layer in the dissipation phase. The integral length scale of dominant eddies can be roughly estimated using a characteristic velocity $\sqrt{e} \sim 1$ m s^{-1} as ~ 10 m for the wavelets of $T < 16$ s and ~ 100 m for $T < 3$ min. Interestingly, these are typical (vertical and horizontal) eddy sizes that determine atmospheric boundary-layer dynamics.

The stable stratification developed due to mixing of warm southerly air and colder northerly air within the low might have kept the TKE low during and after fog formation, as evident from the multi-layer structure observed at 0100 UTC in Fig. 6. The presence of stably stratified turbulence is supported by reckoning the Ozmidov length scale in the lower layers,

$$\left(\frac{\varepsilon}{N^3}\right)^{1/2} \approx \left(\frac{0.03}{0.01^3}\right)^{1/2} \approx 60\,\text{m},$$

N being the Brunt–Väisälä frequency, which is the height of the lowest inversion at 0100 UTC. According to previous studies, the height of a stable-stratification-affected turbulent layer is on the order of the Ozmidov length scale (De Silva and Fernando 1992; Conry et al. 2020).

4.6.3 Sensible Heat Flux

The air–sea sensible heat exchange from 2100 UTC 12 September to 0000 UTC 13 September was small, with a stable surface layer caused by air being warmer than the sea surface, which is expected from air advection from the south (Fig. 6b) and the low wind speed. The sign of the air–sea temperature difference changed at 0030 UTC following the fog genesis, from the ocean surface being colder than the air to warmer than the air, mainly due to colder air rather than an increase of SST. There was significant upward sensible heat flux from the sea surface to the air from the start of the first fog episode at 0000 UTC until 0200 UTC (62% of the event). Then, the sensible heat flux (SHF) switched sign and was negative (downward SHF) for the remaining 38% of the first fog event when the sea surface was warmer, ending at 0315 UTC. The positive heat flux was not fully in sync with periods of colder air overlying warmer water that should have been convection driven by the ocean-air heat flux, but governed by a complex set of processes. In fact, at the time when the positive heat flux developed the ocean was colder and the time when the negative flux developed the ocean was warmer. However, the onset of a positive heat flux was associated with an onset of a positive mean vertical velocity component and the transitioning of a warmer air from the south to a colder air from north. This is similar to the 'paint stripper effect' described by Hunt et al. (2003; see their Fig. 3) wherein the arrival of colder air undercuts and lifts existing warmer air locally, with enhanced mixing and overturning, producing a positive heat flux in the near-surface layer topped by an inversion (between the

shallow colder and warmer air layers). This is consistent with the low-level inversion evidenced by radiosonde profile in Fig. 6d, e. Once the shallow colder flow is established, the wind speed increases (Fig. 5d), TKE rises, and enhanced turbulent mixing occurs between colder air underlying the warmer layer, generating a negative heat flux, as seen in Fig. 11b. This is consistent with the results of wavelet analysis that shows eddies of smaller (time) scales involved in the positive heat flux (16 s $< T <$ 3 min, local mixing at the undercutting front) and larger (time) scales (3 min $< T <$ 10 min) involved in mixing between colder air and warmer air aloft by mechanical turbulence. Accordingly, we postulate that the air–sea temperature difference played a secondary role in establishing an intruding colder layer near the sea surface and its dynamics, and hence in the formation and dissipation of fog.

In the second fog episode (0450 UTC to 0650 UTC 13 September), the difference $T_{air} - T_s$ remained negative (sea warmer) and increased from -0.25 to -1.5 K, and SHF was also increasingly negative (from -10 to -65 Wm^{-2}) with SHF downward. Fog appearance was coincident with the negative heat flux that appeared to be generated due to accelerating winds (Fig. 5d) and high turbulence levels (Fig. 11a) that entrained warmer air across the overlying inversion, bringing warmer air to the ocean surface and creating a negative heat flux. This was consistent with the upward migration (entrainment from below) of the inversion, which continues well past the fog dissipation at 0650 UTC (Fig. 6). Again, we hypothesize that the air–sea temperature difference plays a lesser role in this fog episode, as the turbulence in the fog layer in this case was determined by a saturated air layer capped by an inversion with fluxes within. This was mainly determined by the shear generated turbulence near the surface that interacted with the inversion to produce entrainment and a negative heat flux. It is noteworthy that observed counter-gradient (negative) heat fluxes (e.g., between 0200 and 0500 UTC) have an oscillatory behaviour, which has been observed in stably-stratified flows and during entrainment (Lienhard and Van Atta 1990; Fernando 1991). They even appear in convective boundary layers driven by surface heating (positive heat flux), where a negative heat flux was observed in the vicinity of the inversion due to entrainment (De Roode et al. 2004). It is clear from the radiosonde profiles at 0519, 0623, and 0814 UTC (Fig. 6) that active entrainment was taking place at the inversion bases due to an increase of the wind speed, thus elevating the inversion from 200 to 700 m. We argue that such entrainment was a possible cause of the significant negative fluxes at the bow-mast level.

4.6.4 Latent Heat Flux

For the latent heat flux, larger deviations were observed before 2030 UTC 12 September, which included the precipitation period. However, during the fog event, the latent heat flux remained near zero, although the data were designated low quality and so are not investigated further.

5 Discussion

5.1 Timing with Cyclonic System

An eastward-moving cyclonic system controlled different aspects of the fog. However, it is widely accepted that advection itself (warm air from the south traveling over colder SST) controls fog in Atlantic Canada, which is not so in this case and others that we have

examined. Although the surface winds at the ship were from the south starting at 1200 UTC 12 September, the first fog event began when the low crossed the coast and after the 10-m ship winds were from the north. This first event ended 195 min later when the 6-h, backtracked parcel lifting ceased below 600 m. The second fog event started 90 min later with a reduction in wind speed and vertical velocity component. The second fog event ended 120 min later with decreasing 2-m humidity and increasing TKE as the surface low moved further to the south-east.

5.2 Causes of Fog

The first fog event had fog in the lower layer and two cloud layers above. The lower layer had a 24-h back trajectory (HYSPLIT, Reynold et al. 2002) from the south, but curved around clockwise in the last 3 h of travel to arrive from the north–north-west at the ship after 0000 UTC 13 September. Fog formation was a result of lifting caused by low-level convergence or undercutting of warm air by colder intrusion (Hunt et al. 2003; Koračin et al. 2014) supported by HYSPLIT back trajectories. The formation process was patchy, as shown by the ceilometer image. The middle layer was separated from the lower layer by a saturated air temperature inversion caused by differential advection (Byres 1959). The top layer was the result of a stratus cloud forming and lowering.

The second, later fog event, with a single, shallower layer capped by an inversion may have been caused by the colder saturated air from the north subjected to weakening of winds and hence damping of turbulence. Entrainment at the inversion assisted this process by generating a negative heat (buoyancy flux), and weak turbulence levels promoted droplet growth and maintenance. While the ocean surface was warmer, the heat flux is negative during this fog period, and hence the role of air–sea temperature difference in the formation appears to be secondary. Fog in this layer was also supported by longwave radiation by the top of the layer through the clear sky above (Kim and Yum 2017).

5.3 Boundary-Layer Structure During Two Fog Episodes

Two distinct fog structures are observed in the studied fog event based on the data analysis from on-board instruments presented above. The first fog episode consisted of a surface fog layer capped by a stable complex of neutral layers and air temperature inversions. The first 62% of this fog episode had upward sensible heat flux while the last 38% had downward sensible heat flux.

After a transition period of high visibility, the second fog episode appeared with only one fog layer with a neutrally stable profile capped by an air temperature inversion. Despite the sea being warmer than the air, there was a downward sensible heat flux. Increasing surface wind speed caused increased entrainment at the fog top and a negative heat flux, which ultimately led to fog dissipation.

5.4 Synoptic Overview—Back Trajectories, Structure, and Forcing

The structures and forcing associated with fog episodes analyzed here are complex. Therefore, schematic diagrams are presented as paths and profiles to summarize their relationships.

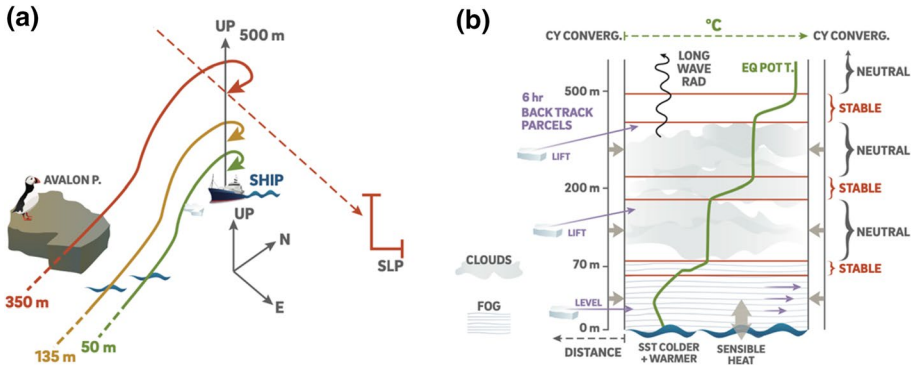

Fig. 12 Schematic of paths and profile of first fog event 0000–0315 UTC 13 September 2018. **a** All backtracks originated in the south, passed the ship to the west, rotated clockwise, arrived at the ship from the north, and travelled over water except for when the 350-m parcel travelled over the Avalon Peninsula, **b** vertical profile showing horizontal surface convergence due to low (convergence), 6-h backtracks above 70-m increased elevation (lift), upward longwave radiation from the top layer, $T_{air}-T_s$ was first positive then negative (changed at ≈0030 UTC 13 September), sensible heat was first downward then upward (changed at ≈0200 UTC 13 September, double arrow)

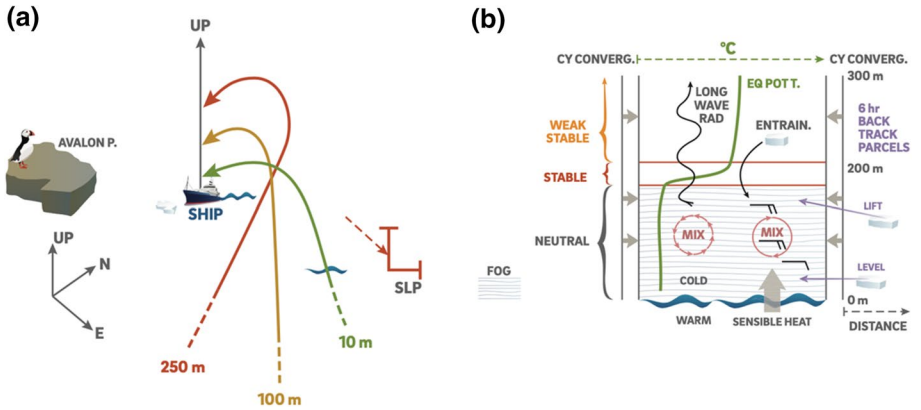

Fig. 13 Schematic of paths and profile of the second fog event 0450–0650 UTC 13 September 2018. **a** All backtracks originated in the south, travelled over water, passed to the east of the ship, rotated counterclockwise, and arrived at the ship from the north, **b** vertical profile showing horizontal surface convergence due to low (convergence), upward longwave radiation was from fog layer, T_{air} was colder than the SST, and sensible heat was upward

For the first fog event, the fog cloud consisted of a surface layer and two thick cloud layers that are represented by back trajectories of air parcels over the ship at 50 m, 135 m, and 350 m. All air parcels travelled from the south as a SLP low approached from the west (Fig. 12a). However, the last 6 h of the 50-m trajectory travelled horizontally over the sea surface, the 135-m air parcel was lifted and traveling a longer distance to the west of the low but still over water. In contrast, the 350-m back trajectory originated farther west, travelling over the Avalon Peninsula. In the last portion of their paths, all parcels moved around in a clockwise, curved arc, arriving over the ship from the north in response to a low centre that was north of the ship moving eastward.

The result was the profile over the ship with three neutral lapse layers and three inversions (Fig. 12b). Contributing to condensation was convergence and lifting by the low, stratus lowering of the upper layer to merge with the middle layer, longwave radiation upward from the top layer, and advection of the still warmer surface layer air moving a short-curved path over colder water and arriving at the ship from the north around 0030 UTC 13 September. Note that at 0030 UTC, the air temperature minus SST reversed. Before 0030 UTC, the air temperature was greater than the SST and after was less than the SST. The sensible heat flux was upward for 0000–0200 UTC and downward for the remainder of this event.

The second fog event continued to be controlled by the low moving farther to the south-east (Fig. 13a). Back trajectories also started in the south but passed the ship to the east and curved counterclockwise to arrive at the ship from the north around 0500 UTC 13 September, all travelled over water and parcels above 10 m increased in elevation. The result was a single saturated surface layer with fog, capped by an inversion (Fig. 13b). The factors contributing to fog were convergence and lifting by the low, longwave radiation upward, mixing of the near sea surface air upward to condensation by colder air moving southward over warmer water arriving at the ship from the north.

6 Conclusions

The goal of this study was to report detailed measurements of marine fog during the event period, or SIOP 1, of the C-FOG field campaign that occurred off the coast of St John's, Newfoundland. The fog occurred at night from 0000 to 0315 UTC 13 September 2018, and 0450–0650 UTC 13 September 2018.

An eastward-moving synoptic scale cyclonic system controlled the synoptic-scale circumstances for the fog. This involved a closed isobar at sea level around the low that included a 2-m RH maximum. Above the low was an open cyclonic wave at 700 hPa and subsidence. When the low crossed the coast, winds rotated from south to west to north and then the first fog event started. A layer of low stratus was present above the fog events.

There were two fog episodes with very different structure and conditions. The first fog event had a surface fog layer capped by two equivalent potential neutral lapse rate cloud layers separated by two saturated air temperature inversions and a subsidence inversion capping the top layer.

The second fog episode was a single equivalent potential neutral lapse rate layer that extended from the sea surface to the top of the layer. This fog layer was three times the height of the first fog layer and capped by a subsidence inversion and dry layer.

During both fog events, there was a low stratus overcast, no upper clouds, longwave upward and no sun. During 0000–1200 UTC 13 September, including during the fog event, there was near-zero latent heat flux, low TKE, winds from the north and 24-h back trajectories originated in the south, consistent with the conditions mentioned in Gultepe et al. (2021) for fog prediction.

During the fog episode, microphysical parameters liquid water content, droplet number concentration, effective diameter, and mean volume diameter evolved over time. A bimodal distribution of fog DSD was observed with modal diameters around 30 μm and 5 μm similar to the pre-fog peak *MVD*. As has been previously observed (Gultepe et al. 2017), the visibility showed an indirect relationship to the droplet number concentration and liquid

water content, however it should be noted that the values of *Nd* in this case are relatively small compared to those in Gultepe et al. (2017).

During the first 30 min of the fog, the 10-m air temperature T_{air} was higher than the SST, and afterwards this reversed for the reminder of the fog events. Thereafter the SST was higher than T_{air} until after the fog events. On the other hand, the sensible heat flux was from air to sea for 62% of the first fog episode and from sea to air for the remainder of the first fog event and continued for the second fog event. The measured heat fluxes are poorly related to the air–sea temperature difference, which plays a lesser role in fog formation and dissipation compared to shear produced turbulence, stratification effects, and entrainment in the lower region of the atmosphere. The negative entrainment heat flux appears to overshadow the influence of cloud top cooling and positive sensible heat flux from the ocean surface to the air.

Overall, our analysis suggests that fog formation during these events was preconditioned and governed by evolving synoptic systems that drive a mix of meso- (transport and horizontal mixing) and small-scale (turbulence and three-dimensional mixing) processes conducive for fog formation. Therefore, the appropriate scale continuum needs to be captured by or accurately parametrized in predictive models for improved fog forecasting. Fernando et al. (2020) presented a case where mesoscale modelling predicted the synoptic and mesoscale details accurately but closely missed the prediction of fog because of the deficiencies of subgrid turbulence parametrizations. Detailed case studies of the type presented here will be useful for identification of physical processes that need to be included in fog parametrizations.

Acknowledgements This research was funded by the Office of Naval Research Award # N00014-18-1-2472 entitled: Toward Improving Coastal Fog Prediction (C-FOG). We thank the crew of the *R/V Hugh R. Sharp* for their outstanding services and Orson Hyde (University of Notre Dame) for his excellent field operational support. We gratefully acknowledge the support in terms of data sharing from Qing Wang and Denny Alappattu (Naval Postgraduate School), Eric Pardyjak and Alexei Perelet (University of Utah), and Baban Nagare (Dalhousie University). *PNNL is operated by Battelle Memorial Institute for the U.S. Department of Energy under Contract DE-AC05-76RL01830.*

References

AMS (2012a) Moist-adiabatic lapse rate—glossary of meteorology. https://glossary.ametsoc.org/wiki/Moist-adiabatic_lapse_rate. Accessed 21 Apr 2021

AMS (2012b) Fog—AMS glossary. http://glossary.ametsoc.org/wiki/Fog. Accessed 25 Sep 2020

AMS (2012c) Equivalent potential temperature—glossary of meteorology. https://glossary.ametsoc.org/wiki/Equivalent_potential_temperature. Accessed 21 Apr 2021

AMS (2012d) Bulk Richardson number—glossary of meteorology. https://glossary.ametsoc.org/wiki/Bulk_richardson_number. Accessed 21 Apr 2021

AMS (2012e) Brunt-Vaisala frequency—glossary of meteorology. https://glossary.ametsoc.org/wiki/Brunt-vaisala_frequency. Accessed 21 Apr 2021

Aubinet M, Vesala T, Papale D (eds) (2012) Eddy covariance: a practical guide to measurement and data analysis. Springer, Dordrecht

Byers HR (1959) General meteorology. McGraw-Hill

Conry P, Kit E, Fernando HJS (2020) Measurements of mixing parameters in atmospheric stably stratified parallel shear flow. Environ Fluid Mech 20:1177–1197. https://doi.org/10.1007/s10652-018-9639-z

Cuxart J, Morales G, Terradellas E (2002) Study of coherent ctructures and estimation of the pressure transport terms for the nocturnal stable boundary layer. Boundary-Layer Meteorol 105:305–328

De Roode SR, Jonker HJJ, Duynkerke PG, Stevens B (2004) Countergradient fluxes of conserved variables in the clear convective and stratocumulus-topped boundary layer: the role of the entrainment flux. Boundary-Layer Meteorol 112:179–196. https://doi.org/10.1023/B:BOUN.0000020167.25780.16

De Silva IPD, Fernando HJS (1992) Some aspects of mixing in a stratified turbulent patch. J Fluid Mech 240:601–625. https://doi.org/10.1017/S0022112092000223
Daubechies I (1992) Ten lectures on wavelets. SIAM
Dorman CE, Koračin D, McEnvoy, (2017) Worldwide marine fog occurrence and climatology. In: Koračin D, Dorman CE (eds) Marine fog challenges and advancements in observations modelling and forecasting. Springer, Berlin, pp 7–152
Draxler, RR, Hess, GD (1997) Description of the HYSPLIT_4 modeling system. NOAA technical memorandum. ERL ARL-224
Dupont JC, Haeffelin M, Protat A, Bouniol D, Boyouk N, Morille Y (2012) Stratus-fog formation and dissipation: a 6-day case study. Boundary-Layer Meteorol 143:207–225. https://doi.org/10.1007/s10546-012-9699-4
Farge M (1992) Wavelet transforms and their applications. Annu Rev Fluid Mech 24:395–457. https://doi.org/10.5860/CHOICE.39-6472
Fernando HJ (1991) Turbulent mixing in stratified fluids. Annu Rev Fluid Mech 23(1):455–493
Fernando HJ, Gultepe I, Dorman C, Pardyjak E, Wang Q, Hock SW, Richter D, Creegan E, Gabersek S, Bullock T, Hocut C, Chang R, Alappattu D, Dimitrova R, Flagg D, Grachev A, Krishnamurthy R, Singh DK, Singh DK, Lozovatsky I, Nagare B, Sharma A, Wagh S, Wainwright C, Wroblewski M, Yamaguchi R, Bardoel S, Coppersmith RS, Chisholm N, Gonzalez GN, Hyde O, Morrizon T, Olson A, Perelet A, Perrie W, Wang S, Wauer B (2020) C-FOG : life of coastal fog. Bull Am Meteor Soc. https://doi.org/10.1175/BAMS-D-19-0070.1
Foken T, Wichura B (1996) Tools for quality assessment of surface-based flux measurements. Agric Forest Meteorol 78:83–105. https://doi.org/10.1016/0168-1923(95)02248-1
Garland JA (1971) Some fog droplet size distributions obtained by an impaction method. Q J R Meteorol Soc 97:483–494. https://doi.org/10.1002/qj.49709741408
Gultepe I, Milbrandt JA (2010) Probabilistic parameterizations of visibility using observations of rain precipitation rate, relative humidity, and visibility. J Appl Meteorol Climatol 49:36–46. https://doi.org/10.1175/2009JAMC1927.1
Gultepe I, Tardif R, Michaelides SC, Cermak J, Bott A, Bendix J, Müller MD, Pagowski M, Hansen B, Ellrod G, Jacobs W, Toth G, Cober SG (2007) Fog research: a review of past achievements and future perspectives. Pure Appl Geophy 164:1121–1159. https://doi.org/10.1007/s00024-007-0211-x
Gultepe I, Pearson G, Milbrandt JA, Hansen B, Platnick S, Taylor P, Gordon M, Oakley JP, Cober SG (2009) The fog remote sensing and modeling field project. Bull Am Meteorol Soc 90:341–359. https://doi.org/10.1175/2008BAMS2354.1
Gultepe I, Fernando HJS, Pardyjak ER, Hoch SW, Silver Z, Creegan E, Leo LS, Pu Z, De Wekker SFJ, Hang C (2016) An overview of the MATERHORN fog project: observations and predictability. Pure Appl Geophy 173:2983–3010. https://doi.org/10.1007/s00024-016-1374-0
Gultepe I, Milbrandt JA, Zhou B (2017) Marine fog: a review on microphysics and visibility prediction. In: Marine fog challenges and advancements in observations modelling and forecasting, pp 345–394
Gultepe I, Heymsfield AJ, Fernando H et al (2021) A review of coastal fog microphysics during C-FOG. Boundary-Layer Meteorol (submitted)
Heo KY, Ha KJ (2010) A coupled model study on the formation and dissipation of sea fogs. Mon Weather Rev 138:1186–1205. https://doi.org/10.1175/2009MWR3100.1
Huang H, Liu H, Huang J, Mao W, Bi X (2015) Atmospheric boundary layer structure and turbulence during sea fog on the Southern China Coast. Mon Weather Rev 143:1907–1923. https://doi.org/10.1175/mwr-d-14-00207.1
Hunt JCR, Fernando HJS, Princevac M (2003) Unsteady thermally driven flows on gentle slopes. J Atmos Sci 60(17):2169–2182
Isaac GA, Bullock T, Beale J, Beale S (2020) Characterizing and predicting marine fog offshore Newfoundland and Labrador. Weather Forecast 35:347–365. https://doi.org/10.1175/WAF-D-19-0085.1
Kim CK, Yum SS (2010) Local meteorological and synoptic characteristics of fogs formed over Incheon international airport in the west coast of Korea. Adv Atmos Sci 27:761–776. https://doi.org/10.1007/s00376-009-9090-7
Kim CK, Yum SS (2017) Turbulence in marine fog. In: Koračin D, Dorman CE (eds) Marine fog challenges and advancements in observations modelling and forecasting. Springer, Berlin, pp 245–273
Kim W, Yum SS, Hong J, Song JI (2020) Improvement of fog simulation by the nudging of meteorological tower data in the WRF and PAFOG coupled model. Atmosphere 11:311. https://doi.org/10.3390/atmos11030311
Koračin D, Dorman CE (2017) Marine fog: challenges and advancements in observations, modeling, and forecasting. Springer

Koračin D, Dorman CE, Lewis JM, Hudson JG, Wilcox EM, Torregrosa A (2014) Marine fog: a review. Atmos Res 143:142–175. https://doi.org/10.1016/j.atmosres.2013.12.012

Kotthaus S, O'Connor E, Münkel C, Charlton-Perez C, Haeffelin M, Gabey AM, Grimmond C (2016) Recommendations for processing atmospheric attenuated backscatter profiles from Vaisala CL31 ceilometers. Atmos Meas Tech 9:3769–3791. https://doi.org/10.5194/amt-9-3769-2016

Krischer L, Megies T, Barsch R, Beyreuther M, Lecocq CC, Wassermann J (2015) ObsPy: a bridge for seismology into the scientific python ecosystem. Comput Sci Discov 8:014003. https://doi.org/10.1088/1749-4699/8/1/014003

Lewis J, Koracin D, Rabin R, Businger J (2003) Sea fog off the California coast: viewed in the context of transient weather systems. J Geophys Res Atmos 108:1–17. https://doi.org/10.1029/2002jd002833

Lienhard JH, Van Atta CW (1990) The decay of turbulence in thermally stratified flow. J Fluid Mech 210:57–112. https://doi.org/10.1017/S0022112090001227

Oliphant AJ, Baguskas SA, Fernandez DM (2021) Impacts of low cloud and fog on surface radiation fluxes for ecosystems in coastal California. Theor Appl Climatol 144:239–252. https://doi.org/10.1007/s00704-021-03518-y

Pedregosa F, Varoquaux G, Gramfort A, Michel V, Thirion B, Grisel O, Blondel M, Prettenhofer P, Weiss R, Dubourg V, Vandeerplas J, Passos A, Cournapeau D, Brucher M, Perro M, Duchesnay E (2011) Scikit-learn: machine learning in python. J Mach Learn Res 12:2825–2830

Petterssen S (1938) On the causes and the forecasting of the California fog. Bull Am Meteorol Soc 19:49–55. https://doi.org/10.1175/1520-0477-19.2.49

Tardif R, Rasmussen RM (2008) Process-oriented analysis of environmental conditions associated with precipitation fog events in the New York City region. J Appl Meteorol Climatol 47:1681–1703. https://doi.org/10.1175/2007JAMC1734.1

Taylor G (1917) The formation of fog and mist. Q J R Meteorol Soc 43:241–268

Tennekes H, Lumley JL (1972) A first course in turbulence, 1st edn. The MIT Press, Cambridge

Terradellas E, Soler MR, Ferreres E, Bravo M (2005) Analysis of oscillations in the stable atmospheric boundary layer using wavelet methods. Boundary-Layer Meteorol 114:489–518. https://doi.org/10.1007/s10546-004-1293-y

Torrence C, Compo GP (1998) A practical guide to wavelet analysis. Bull Am Meteorol Soc 79:61–78

Vaisala (2004) Present weather detector PWD22 user's guide. Vaisala

Authors and Affiliations

S. Wang[1] · H. J. S. Fernando[1,2] · C. Dorman[6,7] · E. Creegan[3] · R. Krishnamurthy[1,4] · C. Wainwright[1] · S. Wagh[1] · R. Yamaguchi[5]

[1] Department of Civil and Environmental Engineering and Earth Sciences, University of Notre Dame, Notre Dame, IN 46556, USA

[2] Department of Aerospace and Mechanical Engineering, University of Notre Dame, Notre Dame, IN 46556, USA

[3] Army Research laboratory, White Sands Missile Range, Las Cruces, NM 88002, USA

[4] Pacific Northwest National Laboratory, Richland, WA 99354, USA

[5] Naval Postgradaute School, Monterey, CA 93943, USA

[6] Integrative Oceanography Division, Scripps Institution of Oceanography, University of California, San Diego, La Jolla, CA 92093-0209, USA

[7] Department of Geological Sciences, San Diego State University, San Diego, CA 92182-1020, USA